*ILASS Americas 22nd Annual Conference on Liquid Atomization and Spray Systems, Cincinnati, OH, May 2010*

# Effect of Grid Spacing in Large-Eddy Simulation of Evaporating Drops in a Mixing Layer

Senthilkumaran Radhakrishnan[1] and Josette Bellan[1,2]
Jet Propulsion Laboratory[1], California Institute of Technology, Pasadena CA 91109-8099
California Institute of Technology[2], Pasadena CA 91125

**Abstract**

Large Eddy Simulation (LES) of a mixing layer with evaporating drops has been performed with various Sub Grid Scale (SGS) models. The objectives of this work are to identify the statistics that are essential for validation of LES, to quantify the accuracy of their prediction by the SGS model and to clarify the grid-spacing influence on the results. Four SGS models namely, the dynamic Smagorinsky (SM) model, the dynamic Gradient (GR) model, the dynamic mixed model which combines SM with a Scale-Similarity term and the dynamic Clark model which combines the SM and GR gradients are tested. A set of first order, second order and drop conditioned statistics from LES predictions are compared to the Direct Numerical Simulation (DNS) results. First order statistics such as Favre averaged streamwise velocity, Favre averaged vapor mass fraction, and the drop streamwise velocity are predicted accurately by all the models tested. Second order statistics such as the streamwise Reynolds stress, the cross-stream Reynolds stress, the spanwise Reynolds stress and the vapor mass fraction fluctuation variance are predicted with a maximum of 15 percent error by the SGS models tested. The dynamic Smagorinsky model predicts the drop conditioned statistics, which describe the segregation of the drops in high strain rate region, more accurately compared to the other models tested. Essentially, only the mean values are grid-spacing independent.

## 1 Introduction

Accurate prediction of multiphase turbulent flows encountered in many applications such as fuel injection and atomization is of utmost importance. Direct Numerical Simulation (DNS) of the governing equations resolves all the flow scales and thus provides the most accurate flow prediction. DNS requires high computational cost and cannot be used in engineering design applications where iterations among several design conditions are necessary. Large Eddy Simulation (LES) provides a cheaper solution although it has modeling requirements compared to DNS. In LES only the energy-containing large scales, which are of engineering interest, are resolved and the more universal small scales are modeled thereby minimizing computational costs. LES equations are obtained through filtering of the Navier-Stokes equations. The effect of the filtered small-scale motion on resolved large scale motion appears as Subgrid-Scale (SGS) terms in the LES equation and it depends on the neglected effects which are unavailable; instead, these terms must be modeled. This modeling is typically done through representing the small-scale terms as functions of the large scale flow field.

To quantify the accuracy of flow predictions by SGS models, LES validation is usually performed using experimental data. The purpose of LES validation is not only to quantify the accuracy of predicted flow for cases where experimental data is available, but to give confidence that the physics in the SGS model is correct so that LES can be used as a predictive tool for cases where experimental data is not available. Often, LES is validated with first- and second-order statistics such as mean velocity and Reynolds stresses, which are predicted reasonably well by many SGS models. One of the objectives of this work is to identify other statistics that are related to drops which are essential for validation of LES of multiphase flows. To quantify the error in LES prediction and to identify the drop related statistics that are appropriate for LES validation, we take DNS as the ideal experiment in which all desired information is available and we compare LES results with those of the DNS. For the purpose of these comparisons, we have created a new DNS database with a much larger number of drops than in the past [1] and with different initial conditions. This DNS database is used to evaluate the accuracy of the LES predictions by various SGS models.

## 2 Governing Equations

The carrier gas phase is treated in an Eulerian framework whereas the dispersed liquid drops are tracked in a Lagrangian framework. The drops are much smaller than Kolmogorov scale and are assumed to be spherical. The volume fraction of the dispersed liquid drops in the carrier gas phase is small (less than $O(10^{-3})$). The drops are treated as point sources for the purpose of calculating the contribution of mass, momentum and energy to the gas phase.

### *2.1 DNS Equations*

The compressible continuity, Navier-Stokes, energy and species conservation equations are solved for the conserved variables density($\rho$), momentum ($\rho u_i$), total energy ($\rho e_t$) and vapor mass fraction ($\rho Y_V$), where $\rho$ is the density, $u_i$ is the velocity in the $x_i$ coordinate direction, $e_t$ is the total energy, $Y_V$ is the mass fraction of the vapor and $Y_C$ is the mass fraction of the carrier gas (Note $Y_C + Y_V = 1$). The governing equations are

$$\frac{\partial \rho}{\partial t} + \frac{\partial (\rho u_i)}{\partial x_i} = S_{mass}, \tag{1}$$

$$\frac{\partial (\rho u_i)}{\partial t} + \frac{\partial (\rho u_i u_j)}{\partial x_j} = -\frac{\partial p}{\partial x\, i} + \frac{\partial \sigma_{ij}}{\partial x_j} + S_{mom,i}, \tag{2}$$

$$\frac{\partial (\rho e_t)}{\partial t} + \frac{\partial (\rho e_t u_j)}{\partial x_j} = -\frac{\partial (p u_i)}{\partial x_i} + \frac{\partial q_i}{\partial x_i} + \frac{\partial (\sigma_{ij} u_i)}{\partial x_j} + S_{energy}, \tag{3}$$

$$\frac{\partial (\rho Y_V)}{\partial t} + \frac{\partial (\rho Y_V u_j)}{\partial x_j} = -\frac{\partial j_{Vj}}{\partial x_j} + S_{mass}, \tag{4}$$

The sources terms ($S_{mass}$, $S_{mom,i}$ and $S_{energy}$) which appear in eqs. 1-4 describe the exchange of mass, momentum and energy between the two phases. Both the carrier gas and the vapor are assumed to be perfect gases and the perfect gas equation is used to relate the pressure ($p$) and the temperature ($T$),

$$p = \rho R T, \tag{5}$$

where $R = Y_V R_V + Y_C R_C$, $R_V = R_u/m_v$, $R_C = R_u/m_C$, $R_u$ is the universal gas constant, $m_C$ and $m_V$ are the molar weights of the carrier gas and the vapor respectively. The total enthalpy ($h$) is the sum of the enthalpies of the carrier gas and the vapor,

$$h = h_V Y_V + h_C Y_c, \tag{6}$$

where $h_C$ and $h_V$ are the enthaplies of the pure gases. We assume that the specific heat capacities of the gases are constant in the small variation of the pressure and temperature observed in the flow.

The temperature ($T$) is computed from the total energy($e_t$) through

$$e_t = C_v T + h_V^0 Y_V + \frac{1}{2} u_i u_i. \tag{7}$$

The viscous stresses ($\sigma_{ij}$) are computed using

$$\sigma_{ij} = 2\mu \left( S_{ij} - \frac{1}{3} S_{kk} \delta_{ij} \right), \tag{8}$$

where $\mu$ is the coefficient of viscosity and $S_{ij}$ is the rate of the strain

$$S_{ij} = \frac{1}{2} \left( \frac{\partial u_i}{\partial x_j} + \frac{\partial u_j}{\partial x_i} \right). \tag{9}$$

The vapor mass flux in eq. 4 in and heat flux in eq. 3 are computed using

$$\begin{aligned} j_{Vj} &= \rho Y_V V_{Vj} = -\rho Y_V \{ \frac{D}{Y_V} \frac{\partial Y_V}{\partial x_j} \\ &+ Y_C \left( Y_V + Y_C \frac{m_V}{m_C} \right) \left[ \frac{m_C}{m_V} - 1 \right] \frac{D}{p} \frac{\partial p}{\partial x_j} \}, \end{aligned} \tag{10}$$

$$q_j = -\lambda \frac{\partial T}{\partial x_j} + (h_V - h_C)\, j_{Vj}, \tag{11}$$

where $V_{Vj}$ is the vapor diffusion velocity, $D$ is the diffusion coefficient and $\lambda$ is the thermal conductivity. In eqs. 8,10 and 11, $\mu$, $D$ and $\lambda$ are assumed to be constants and are related through the specified Prandtl ($Pr = 0.7$) and Schmidt numbers ($Sc = 0.7$).

The governing equations for an individual drop describing the evolution of its position ($X_i$), velocity ($v_i$), temperature ($T_d$) and the mass ($m_d$) are

$$\frac{dX_i}{dt} = v_i, \tag{12}$$

$$m_d \frac{dv_i}{dt} = F_{drag,i}, \tag{13}$$

$$m_d C_L \frac{dT_d}{dt} = Q \quad + \frac{dm_d}{dt} L_V, \tag{14}$$

$$\frac{dm_d}{dt} = \dot{m_d}, \tag{15}$$

where $F_{drag,i}$ is the drag force, $Q$ is the heat flux from the gas phase to drop, $\dot{m_d}$ is the evaporation rate, $C_L$ is the heat capacity of the drop liquid and $L_V$ is the latent heat of vaporization. The expressions for the drag, heat flux and the evaporation rate involve the use of the following validated models for the description of a single drop behavior:

$$F_{drag} = \frac{m_d}{\tau_d} f_1 \left( u_i - v_i \right), \tag{16}$$

$$Q = \frac{m_d}{\tau_d} \frac{Nu}{3Pr} C_p f_2 (T - T_d), \tag{17}$$

$$\frac{dm_d}{dt} = -\frac{m_d}{\tau_d} \frac{Sh}{3Sc} \ln[1 + B_M], \tag{18}$$

where $C_p$ is the gas heat capacity at constant pressure and $\tau_d$ is the particle time constant given by

$$\tau_d = \frac{\rho_l d^2}{18\mu}, \tag{19}$$

with $\rho_l$ being the density of the drop liquid and $d$ being the drop diameter. More details about the empirical correlations such as $f_1$, $f_2$, the Nusselt number $Nu$, the Schmidt number $Sh$ etc. that appear in eqs. 16-18 can be obtained in Okongo and Bellan[1], and Miller and Bellan[2].

Since the point source approximation is used, the contribution from each of the drops to the mass, momentum and the energy of the gas phase is described by the following equations:

$$S_{mass,d} = -\frac{dm_d}{dt}, \tag{20}$$

$$S_{mom,i,d} = -\left[ F_{drag,i} + \frac{dm_d}{dt} v_i \right], \tag{21}$$

$$S_{energy,d} = -\left[ F_{drag,i} v_i + \frac{dm_d}{dt} \left( \frac{1}{2} v_i v_i + h_V \right) \right], \tag{22}$$

### *2.2 LES Equations*

LES equations are obtained by low-pass filtering the Navier-Stokes equations, and are solved for the filtered flow field. We define the filtered vector of primitive variables $\overline{\psi}$ as well as the Favre filtered equivalent quantities $\tilde{\psi} \equiv \overline{\rho\psi}/\overline{\rho}$, given the compressible nature of the flow. Thus, whereas in DNS the equations are solved for the conservative variable vector $\phi$, in LES, the equations are solved for the filtered conservative variable vector $\overline{\phi}$. The filtered governing equations are

$$\frac{\partial \overline{\rho}}{\partial t} + \frac{\partial (\overline{\rho} \tilde{u}_i)}{\partial x_i} = \overline{S}_{mass}, \tag{23}$$

$$\frac{\partial (\overline{\rho} \tilde{u}_i)}{\partial t} + \frac{\partial (\overline{\rho} \tilde{u}_i \tilde{u}_j)}{\partial x_j} = -\frac{\partial p(\overline{\phi})}{\partial x_i} + \frac{\partial \sigma_{ij}(\overline{\phi})}{\partial x_j} + \overline{S}_{mom,i} - \frac{\partial \tau_{ij}}{\partial x_j}, \tag{24}$$

$$\frac{\partial (\overline{\rho} \tilde{Y_v})}{\partial t} + \frac{\partial (\overline{\rho} \tilde{Y_v} \tilde{u}_j)}{\partial x_j} = -\frac{\partial j_{Vj}(\overline{\phi})}{\partial x_j} + \overline{S}_{mass} - \frac{\partial \eta_j}{\partial x_j}, \tag{25}$$

$$\begin{aligned} \frac{\partial (\overline{\rho} \tilde{e}_t)}{\partial t} + \frac{\partial (\overline{\rho} \tilde{e}_t \tilde{u}_j)}{\partial x_j} &= -\frac{\partial (\overline{\rho} \tilde{u}_i)}{\partial x_i} + \frac{\partial q_i(\overline{\phi})}{\partial x_i} + \frac{\partial \left[ \sigma_{ij} \left( \overline{\phi} \right) \tilde{u}_i \right]}{\partial x_j} \\ &+ \overline{S}_{energy} - \frac{\partial \zeta_j}{\partial x_j} - \frac{\partial (\tau_{ij} \tilde{u}_i)}{\partial x_j}. \end{aligned} \tag{26}$$

Filtering has introduced additional SGS terms namely SGS stresses $\tau_{ij}$, and SGS scalar fluxes $\eta_j$ and $\zeta_j$. The expressions for these SGS terms are:

$$\tau_{ij} = \overline{\rho}\left(\widetilde{u_i u_j} - \tilde{u}_i\tilde{u}_j\right), \tag{27}$$

$$\zeta_j = \overline{\rho}\left(\widetilde{hu_j} - \tilde{u}_j\tilde{h}\right), \tag{28}$$

$$\eta_j = \overline{\rho}\left(\widetilde{Y_V u_j} - \tilde{u}_j\tilde{Y_V}\right). \tag{29}$$

Note that the above SGS terms represents the effect of the filtered small scale motion on the resolved large scale motion and cannot be directly computed since they depend on information lost upon filtering. Instead, they must be computed from the LES flow using SGS models. Various SGS models used in this work is described in section 2.3.

Filtering has also modified the source terms representing the contribution of mass, momentum and energy from the drops to the gas. These terms are non-linear and present the same modeling difficulty as other non-linear terms in the governing equations in that to be exact, they should be calculated with the unfiltered flow field and then filtered. Since the unfiltered flow field is not available in LES, the filtered source terms are calculated using the filtered flow field with, as a first approximation, with no additional contributions from the neglected scales. Another approximation is used to reduce the number of drops tracked in the LES formulation; each computational drop in the LES calculation actually represent the effect of $N_R$ physical drops. The computational drop field is obtained by dividing the physical number of drops $N_d$ by a factor $N_R$; more details about the LES formulation can be obtained from Leboissetier et al. [3] and Okong'o et al. [4].

### *2.3 LES models*

**Smagorinsky model**

The Smagorinsky [5] (SM) model is an eddy viscosity model derived assuming that the production of the subgrid scale turbulent kinetic energy is in balance with the dissipation of the subgrid scale turbulent kinetic energy. The expression for SGS stress is

$$\begin{aligned}\tau_{ij} - \frac{\delta_{ij}}{3}\tau_{kk} &= -2C_{SM\sigma}\Delta^2\overline{\rho}|S(\overline{\phi})| \\ &\quad\times\left(S_{ij}(\overline{\phi}) - \frac{\delta_{ij}}{3}S_{kk}(\overline{\phi})\right).\end{aligned} \tag{30}$$

Yoshizawa [6] proposed the following model to calculate the SGS turbulent kinetic energy (i.e. the $\tau_{ij}$ trace)

$$\tau_{kk} = 2C_I\Delta^2\overline{\rho}|S(\overline{\phi})|^2, \tag{31}$$

which is used in conjunction with the above SM model. The other SGS fluxes (vapor fraction or enthalpy) are similarly modeled, using the following equation

$$\begin{aligned}\eta_j &= -C_{SMY}\Delta^2\overline{\rho}|S(\overline{\phi})|\frac{\partial Y_v(\overline{\phi})}{\partial x_j}, \\ \zeta_j &= -C_{SMh}\Delta^2\overline{\rho}|S(\overline{\phi})|\frac{\partial h(\overline{\phi})}{\partial x_j}.\end{aligned} \tag{32}$$

**Gradient model**

Gradient (GR) models are derived using a Taylor series expansion for the filtered terms [7, 8]. For the SGS stresses,

$$\tau_{ij} = C_{GR\sigma}\Delta^2\overline{\rho}\frac{\partial\tilde{u_i}}{\partial x_k}\frac{\partial\tilde{u_j}}{\partial x_k}, \tag{33}$$

whereas for the other SGS fluxes (vapor fraction or enthalpy)

$$\begin{aligned}\eta_j &= -C_{GRY}\Delta^2\overline{\rho}\frac{\partial Y_v(\overline{\phi})}{\partial x_k}\frac{\partial\tilde{u_j}}{\partial x_k}, \\ \zeta_j &= -C_{GRh}\Delta^2\overline{\rho}\frac{\partial h(\overline{\phi})}{\partial x_k}\frac{\partial\tilde{u_j}}{\partial x_k}.\end{aligned} \tag{34}$$

**Mixed model**

The mixed model uses the Scale-Similarity (SS) formulation in addition to the SM model. Scale-Similarity postulates that there is a similarity between the smallest resolved scales and the largest unresolved scales, so that a test filter of width $\widehat{\Delta}$ is introduced, $\widehat{\Delta}/\Delta > 1$, and the behavior of the later scales is inferred from the former within this test filter length scale. The SS term has the same mathematical form as the SGS term but the flow field variable is replaced by the filtered flow field. The formulation for the SGS stresses is

$$\begin{aligned}\tau_{ij} - \frac{\delta_{ij}}{3}\tau_{kk} &= -2C_{SM\sigma}\Delta^2\overline{\rho}|S(\overline{\phi})| \\ &\quad\times\left(S_{ij}(\overline{\phi}) - \frac{\delta_{ij}}{3}S_{kk}(\overline{\phi})\right) \\ &\quad+\overline{\rho}\left(\widehat{\tilde{u}_i\tilde{u}_j} - \widehat{\tilde{u}}_i\widehat{\tilde{u}}_j\right),\end{aligned} \tag{35}$$

and for the other SGS fluxes

$$\begin{aligned}\eta_j &= -C_{SMY}\Delta^2\overline{\rho}|S(\overline{\phi})|\frac{\partial Y_v(\overline{\phi})}{\partial x_j} + \overline{\rho}\left(\widehat{\tilde{Y}_V\tilde{u}_j} - \widehat{\tilde{Y}_V}\widehat{\tilde{u}}_j\right), \\ \zeta_j &= -C_{SMh}\Delta^2\overline{\rho}|S(\overline{\phi})|\frac{\partial h(\overline{\phi})}{\partial x_j} + \overline{\rho}\left(\widehat{\tilde{h}\tilde{u}_j} - \widehat{\tilde{h}}\widehat{\tilde{u}}_j\right).\end{aligned} \tag{36}$$

The theoretical value of the proportionality coefficient in the SS model is generally taken to be unity in order to satisfy Galilean invariance.

**Clark model**

The Clark model uses the combination of the SM and GR models to compute the SGS terms. The formulation for the SGS stresses is

$$\begin{aligned}\tau_{ij} - \frac{\delta_{ij}}{3}\tau_{kk} &= -2C_{SM\sigma}\Delta^2\overline{\rho}|S(\overline{\phi})| \\ &\quad \times \left(S_{ij}(\overline{\phi}) - \frac{\delta_{ij}}{3}S_{kk}(\overline{\phi})\right) \\ &\quad + \frac{1}{12}\Delta^2\overline{\rho}\frac{\partial\widetilde{u}_i}{\partial x_k}\frac{\partial\widetilde{u}_j}{\partial x_k}, \end{aligned} \tag{37}$$

and for the SGS fluxes

$$\begin{aligned}\eta_j &= -C_{SMY}\Delta^2\overline{\rho}|S(\overline{\phi})|\frac{\partial Y_v(\overline{\phi})}{\partial x_j} \\ &\quad + \frac{1}{12}\Delta^2\overline{\rho}\frac{\partial Y_v(\overline{\phi})}{\partial x_k}\frac{\partial\widetilde{u}_j}{\partial x_k}, \\ \zeta_j &= -C_{SMh}\Delta^2\overline{\rho}|S(\overline{\phi})|\frac{\partial Y_v(\overline{\phi})}{\partial x_j} \\ &\quad + \frac{1}{12}\Delta^2\overline{\rho}\frac{\partial Y_v(\overline{\phi})}{\partial x_k}\frac{\partial\widetilde{u}_j}{\partial x_k}, \end{aligned} \tag{38}$$

where the GR model is used with the theoretical coefficient value of 1/12, found from the Taylor expansion.

**Dynamic models**

All SGS expressions contain coefficients which must be specified to calculate the SGS terms. *Ad hoc* specification or specification of even tuned values from DNS data bases of these coefficients to a constant value often results in the poor performance or limited value of these models. Germano et al. [9] proposed a dynamic procedure to calculate these coefficients based on the local state of the flow. In this study, all coefficients have been computed using the dynamic approach. Details about the computation of the coefficients for compressible flow can be obtained in Martin et al. [10].

## 3 Numerical methods

Direct Numerical Simulations were performed using a fourth-order explicit Runge-Kutta scheme for temporal integration, an eighth-order central finite differencing scheme for spatial discretization and with a sixteenth-order filter to remove aliasing errors [11]. The non-linear terms in the governing equation were recast in cubic skew symmetric form, as proposed by Kennedy and Gruber [12], to reduce aliasing error. A fourth-order Lagrange interpolation procedure is used to obtain gas-phase variable values at the drop locations [2]. The same numerical scheme is used in LES to ensure that any differences in LES results from the filtered DNS is due to modeling errors rather than numerical errors.

## 4 Problem formulation

The physical configuration is that of a temporal mixing layer having streamwise ($x_1$), the cross-stream ($x_2$), and the spanwise ($x_3$) dimension of 0.6m, 0.45m and 0.15m respectively. Periodic boundary conditions are used in the $x_1$ and $x_3$ directions, and adiabatic slip wall condition [13] is used at the $x_2$ boundaries. Drops reaching the slip walls are assumed to stick to the wall, but are otherwise transported according to the drop equations. Initially, the gas phase consists only of the carrier gas (air with no vapor); the initial mean streamwise velocity has an error-function profile. To promote transition to turbulence, the layer is initially perturbed with homogeneous turbulence [14]. A total number of 71,411,456 n-decane drops, corresponding to a mass load (ratio of liquid mass to the carrier gas mass) of 0.2, are initially distributed randomly throughout the bottom half ($x_2 < 0$) of the domain; the initial velocity of each drop is the same as that of the gas phase at its location. The drops are at a temperature of 345 K which is lower than the boiling point (447.7 K) of n-decane, and also lower than the temperature of air (375 K). The drop size variation is specified by a normal distribution such that the initial Stokes number ($\tau_d \Delta U_0/\delta_{\omega,0}$) mean is 3 and the standard deviation is 0.5.

DNS were performed for an initial vorticity thickness based Reynolds number $Re_0 = \rho_0 \Delta U_0 \delta_{\omega,0}/\mu$, of 1200 and the convective Mach number ($M_{c,0}$) of 0.35, where $\rho_0$ is the initial gas density and $\Delta U_0 = 2U_0$ is the velocity difference across the layer, $U_0 = M_{c,0} a_{C,0}$, is calculated from the specified value of $M_{c,0}$ based on the carrier gas initial speed of sound $a_{C,0}$, and $\delta_{\omega,0} = \delta_\omega(0)$ is the initial vorticity thickness where $\delta_\omega(t) = \Delta U_0 / \left(\partial \langle u_1 \rangle / \partial x_2\right)_{\max}$, $u_1$is the streamwise velocity, where $\langle \quad \rangle$ denotes homogeneous plane averaging, and initially $\langle u_1 \rangle$ has an error-function profile. The DNS grid has 1120 $\times$ 840 $\times$ 280 nodes in the streamwise, cross-stream and spanwise directions respectively. The simulation was performed up to a non-dimensional time, $t^* \equiv t\Delta U_0/\delta_{\omega,0} = 250$. Up to $t^* = 100$, the coupling between drops and gas phase is restricted to momentum and energy transfer due to drag on drops; the drops are neither allowed to evaporate nor to exchange heat with the gas phase until that time. As the flow becomes fully turbulent at $t^* = 100$ and the drops have adjusted to turbulence and preferentially segregated in the high-strain region, they are allowed to evaporate and the full coupling of mass, momentum and energy is enabled.

The initial condition for the LES calculation is the filtered DNS data at $t^* = 100$. Large Eddy Sim-

ulations were performed on three meshes to evaluate the dependence of the results on the choice of the grid. As already stated, in all LES calculations, each computational drop represents 8 physical drops. The resolution used in the calculations are summarized in Table 1. LES calculations were performed on all three grids with each of the four subgrid models described in the previous section.

Because experimental results cannot be used for comparison with a temporal mixing layer, the DNS data will be used here instead. Currently, there is still a controversy as to the best way to compare LES with DNS-obtained results. While on one hand it would be desirable to reproduce DNS data, on the other hand what is computed in LES is a filtered flow field which cannot claim to reproduce the unfiltered flow field; this is particularly true when coarse LES grids are used. However, filtering the DNS database entails the choice of both a filter shape and a filter width. Since in the LES equation derivation the filter shape is generic, i. e. not explicitly specified, and only the filter width appears in SGS models, it seems controversial to compare LES with filtered DNS because the shape of the filter may influence the assessment of how well the LES compares to the DNS-filtered results. That is, in the LES calculation, we do not know the shape of the implicit filter. Given the dependency of the filtered DNS results on the filter shape, and the present focus on SGS models, we choose here to compare the 12 LES calculations to the DNS with the understanding that for coarser LES grids the expectations for good agreement may be reduced.

## 5 Results

The first focus is on integral quantities such as the evolution of momentum thickness and the number of remaining drops. The momentum thickness ($\theta$) measures the growth of the mixing layer and for LES is defined by

$$\theta = \frac{1}{\rho_0 \Delta U_0^2} \int_{-L_2}^{L_2} [\rho \left( 0.5\Delta U_0 - \frac{\langle \overline{\rho} \widetilde{u}_1 \rangle}{\langle \overline{\rho} \rangle} \right) \times \left( 0.5\Delta U_0 + \frac{\langle \overline{\rho} \widetilde{u}_1 \rangle}{\langle \overline{\rho} \rangle} \right)] dx_2. \quad (39)$$

Results from the fine mesh calculation with various models are shown in figure 1. Figure 1a shows the $\theta$ evolution: it increases slowly during the transition stage and follows a linear growth after the flow has fully transitioned to turbulence. All 12 calculations accurately predict the $\theta$ growth. Figure 1b shows the fraction of drops not entirely evaporated, where $N_{drops}$ is the number of droplets at a specified time and $N_{drops,0}$ is the number of drops present at $t^* = 0$. The ratio $N_{drops}/N_{drops,0}$ is also accurately predicted by all models.

Because the mixing layer is homogeneous along the streamwise and spanwise directions, statistics such as mean flow variables, Reynolds stresses etc. can be obtained by averaging along these directions. When the cross-stream coordinate is normalized by the instantaneous momentum thickness (see Rogers and Moser [15]), the flow evolution is self-similar, i.e. the statistical profiles along cross-stream direction is invariant with time during the linear growth stage of the mixing layer. This self-similar property provides another direction (time) for averaging data so as to obtain smooth statistics. All statistics discussed in the following are from averaging both along the $(x_1, x_3)$ directions and in time between $t^* = 150$ to $t^* = 250$; these statistics are presented as a function of the normalized coordinate $\xi = x_2/\theta$.

### *5.1 Effect of resolution*

Results from the three resolutions are compared to check the effect of mesh size on the accuracy of the predicted flow field. Figure 2 depicts the results of calculations with the dynamic SM model. The Favre averaged streamwise velocity is accurately predicted even by the coarse mesh calculation. The Favre-averaged vapor mass fraction is predicted reasonably well at all three resolutions, with the results from the fine mesh showing the best agreement. The Reynolds stresses and the variance of the vapor mass-fraction fluctuations do not show a grid independence. For example, the cross-stream and spanwise Reynolds stresses show a better match with DNS prediction as the resolution increases whereas the streamwise Reynolds stress and the vapor mass-fraction fluctuation are better predicted with the coarse mesh while the fine mesh results show reasonable agreement with the DNS results. Considering the accuracy of all the quantities, the fine mesh calculation lead a more accurate prediction.

Figure 3 illustrates the results of calculations with the dynamic GR model. Mean quantities such as Favre-averaged streamwise velocity and Favre-averaged vapor mass fraction are predicted reasonably well on all three meshes, similar to their prediction by the dynamic SM model. Akin to the SM predictions, grid independent solutions are not obtained with the GR model either. The Reynolds-stress prediction on the fine mesh exhibits the best match with the DNS data. Results of calculations with the dynamic mixed model (SM and SS) are displayed in figure 4. The mixed model shows the same trend as the dynamic SM model for the prediction of various quantities as a function of the resolution.

The peak values of the Reynolds stresses and mass-fraction fluctuation variance are lower than the DNS values. The dynamic Clark model (SM and GR) predictions are illustrated in figure 5. The Reynolds stresses show better agreement with the DNS values at higher resolution while all Reynolds stresses predicted using the fine mesh show reasonable agreement with the DNS values.

Figure 6 presents the one-dimensional streamwise spectra of turbulent kinetic energy and vapor mass fraction fluctuation for the three calculations using the dynamic SM model. As expected, increasing the resolution increases the range of the computed scales. At the coarse resolution, the smallest resolved scales have much lower energy than the DNS whereas at the fine resolution, the smallest resolved scales have as much energy as the DNS. The dynamic SM model is more dissipative at the smallest resolved scales at coarse resolution; increasing the resolution results in more accurate dissipation of the smallest resolved scales. All other models display the same trend (not shown).

The conclusion is that none of the four models exhibits grid independence. Because when the resolution is increased in LES the range of resolved small scales resolved also increases, to obtain grid independence, the range of resolved scales should be fixed while varying the resolution. This can only be achieved if an explicit filter is applied to remove all the scales larger than the filter width.

### *5.2 Effect of the SGS model*

As discussed above, most of the models show the best prediction on the fine mesh. Therefore, it is best compare the results of all the models on the fine mesh. Figure 7 shows the Reynolds stresses and the variance of the vapor mass fraction fluctuation. The dynamic Clark model predicts the streamwise Reynolds stress accurately while all the other models under-predict it. The cross-stream Reynolds stress is predicted reasonably well by all the models, with the dynamic GR model showing the best agreement with the DNS results. The dynamic Clark model predicts the spanwise Reynolds stress accurately while the dynamic SM over-predicts it. All models under-predict the variance of the vapor mass fraction fluctuation. The percentage error in the peak prediction of Reynolds stresses by various models, calculated as

$$\begin{matrix}\%\text{ error} \\ \text{in peak}\end{matrix} = \frac{\text{Predicted peak} - \text{DNS peak}}{\text{DNS peak}} \times 100\%, \tag{40}$$

is listed in Table 2.

Figure 8 displays the one-dimensional streamwise spectra of turbulent kinetic energy and vapor mass fraction fluctuation for all the four models. The dynamic mixed model is more dissipative in the smallest resolved scales compared to the other three models. Both the dynamic SM and the dynamic GR models show good agreement with the DNS spectra up to the smallest resolved scales.

Two-point streamwise correlation of the streamwise velocity and vapor mass fraction fluctuation, are defined as

$$R_{uu}\left(x_3\right) = \frac{< u^{'}\left(x_{1,0}, x_{2,0}, x_{3,0}\right) u^{'}\left(x_{1,0}, x_{2,0}, x_{3,0}+x_3\right) >}{< u^{'}\left(x_{1,0}, x_{2,0}, x_{3,0}\right) u^{'}\left(x_{1,0}, x_{2,0}, x_{3,0}\right) >}, \tag{41}$$

$$R_{Y_vY_v}\left(x_3\right) = \frac{< y_v^{'}\left(x_{1,0}, x_{2,0}, x_{3,0}\right) y_v^{'}\left(x_{1,0}, x_{2,0}, x_{3,0}+x_3\right) >}{< y_v^{'}\left(x_{1,0}, x_{2,0}, x_{3,0}\right) y_v^{'}\left(x_{1,0}, x_{2,0}, x_{3,0}\right) >}, \tag{42}$$

show approximately how far the fluctuation at one point is correlated to the fluctuation as one moves away from the specified point along the streamwise direction. For example, a non-zero two point correlation over a long streamwise distance implies that the streamwise fluctuation are also correlated over a long distance. Figure 9 compares the two point streamwise correlation predicted by all the models to the DNS values. All models show reasonable agreement with the DNS profile.

Figure 10 illustrates the drop statistics such as mean streamwise velocity and the average square of the drop diameter. All models accurately predict both the mean velocity and the square of the diameter in the lower stream. In the upper stream, the dynamic SM model better reproduces the drop statistics whereas the dynamic mixed model shows poor agreement with the DNS results.

In certain multiphase flow applications, such as combustion, the flow field morphology is of high interest because it influences the drop distribution, the species flux directionality, etc. that affect the location of flame structures. To probe the topology of the flow field and inquire whether drops are located in strain or vortical regions, a criterion based on a scalar, $Q$,

$$Q = -\frac{1}{2}\left(\frac{\partial u_i}{\partial x_j}\frac{\partial u_j}{\partial x_i}\right) = -\frac{1}{2}\left(S_{ij}S_{ij} - \Omega_{ij}\Omega_{ij}\right), \tag{43}$$

is used where $\Omega_{ij}$ is the rotation-rate tensor. In regions where the vorticity dominates over the strain-rate, $Q$ is positive and in regions where the strain-rate dominates over the vorticity, $Q$ is negative. The Stokes number ($St_{ave}$) based on Kolmogorov time scale, defined as the ratio of particle response time, $\tau_p$, to the Kolmogorov time scale, $\tau_k$, is often used to identify drop preferential segregation [16]. Drops having $St_{ave} \approx 1$ tend to preferentially segregate in

the low vorticity and high strain rate region due to their inertia. Drops having $St_{ave} < 1$ tend to follow the fluid as a tracer particle. Figure 11 shows $St_{ave}$ conditioned on $Q$, and the number of drops on a $(x_1, x_3)$ slice of thickness $2\Delta_{x2,DNS}$ (twice the grid spacing along $x_2$ direction in the DNS calculation) at $x_2 = 0$, as a function of $Q$. Most drops are in regions where $Q < 0$. As $St_k$ increases and approaches unity, the drops tend to congregate in higher-strain/lower-vorticity regions. In comparison with DNS, all the LES models predict more drops in the region where the vorticity rate and the strain rate are equal, and less drops in the region where the strain rate is high. The dynamic Smagorinsky model predicts the flow-conditioned statistics of drops better than the dynamic mixed and the dynamic gradient models.

## 6 Conclusions

Large Eddy Simulations with various SGS models at three resolutions were performed computing the evolution of a mixing layer having initially one stream laden with evaporating drops. Mean quantities such as Favre averaged streamwise velocity, Favre averaged vapor mass fraction, mean drop streamwise velocity etc. are predicted accurately by all models at all three resolutions. At the coarse resolution, all models are excessively dissipative at the smallest resolved scales. Increasing the resolution results in more accurate dissipation prediction at the smallest resolved scales. Even at the finest resolution tested, at the smallest resolved scale the dynamic mixed model is more dissipative compared to the dynamic SM model. Two-point streamwise correlations of the streamwise velocity and the vapor mass fraction fluctuations are predicted accurately by all models. Drop statistics conditioned with $Q$ describing the preferential segregation of drops are better predicted by the dynamic SM model. The dynamic Clark model predicts the Reynolds stress better than all other models. The variance of the vapor mass fraction fluctuation is predicted with less than 6% error by the dynamic SM model. For LES validation, all second order quantities and the drop conditioned statistics are more important than the first order statistics which are accurately predicted by all the models.

To evaluate LES with respect to experimental data, the expectation is that LES results should be grid independent so that errors in LES prediction should only stem from modeling error, and not be due to truncation or aliasing error. In the present calculation where the filter width is set equal to the grid spacing, the second order statistics were not grid independent. An explicit filter should be applied while refining the grid so that the filter width is kept constant and the range of the scales resolved at different resolution is the same. Calculations using explicit filters are underway to obtain grid-spacing independent results. These calculations will provide a better estimate of model-due errors in predicting various flow statistics.

**Acknowledgments**

This study was conducted at the Jet Propulsion Laboratory (JPL), California Institute of Technology (Caltech) and sponsored by NASA jointly under the Fundamental Aeronautics Program with Drs. Dan Bulzan and Nan-Suey Liu serving as program monitors, and under the LASER program in the ESMD/Advanced Capabilities Division.

**References**

[1] Okong'o, N. and Bellan, J., *J. Fluid Mech.* 499:1–47 (2004).

[2] Miller, R.S. and Bellan, J.,*J. Fluid Mech.* 384:293-338 (1999).

[3] Leboissetier, A., Okong'o, N. and Bellan J., *J. Fluid Mech.*523:37-78 (2005).

[4] Okong'o, N., Leboissetier, A. and Bellan, J., *Phys of Fluids* 20(10):103305 (1-16) (2008).

[5] Smagorinsky, J., *Mon. Weather Rev.* 91:99-164 (1963).

[6] Yoshizawa, A., *Phys. Fluids* 29(7):2152–2164 (1986).

[7] Clark, R., Ferziger, J., and Reynolds, W., *J. Fluid Mech.*91(1):1–16 (1979).

[8] Liu, S., Meneveau, C. and Katz, J., *J. Fluid Mech.*275:83–119 (1994).

[9] Germano, M., Piomelli, U., Moin, P., and Cabot, W., *Phys. Fluids A* 3:1760-1765 (1991).

[10] , Martin, M.P., Piomelli, U. and Candler, G.V., *Theor. and Comp. Fluid Dyn* 13:361-376 (2000).

[11] Kennedy, C. and Carpenter, M., *Appl. Num. Math.* 14:397–433 (1994).

[12] Kennedy, C.A. and Gruber, A., *J. of Comp Phys* 227(3):1676-1700 (2008).

[13] Poinsot, T.J. and Lele, S.K., *J. Comp. Phys.* 101(1):104-129 (1992).

[14] Pantano, C. and Sarkar, S., *J. Fluid Mech.* 451:329-371 (2002).

[15] Rogers, M.M. and Moser, R.D., *Phys. Fluids A* 6(2):903-923 (1994).

[16] Squires, K.D., and Eaton, J.K., *Phys. Fluids A* 3:1169-1178 (1991).

| Calculation | Resolution (Streamwise × Cross-stream × Spanwise) | Number of drops | $N_R$ |
|---|---|---|---|
| LES coarse mesh | 140 × 105 × 35 | 8,926,432 | 8 |
| LES medium mesh | 280 × 210 × 70 | 8,926,432 | 8 |
| LES fine mesh | 560 × 420 × 140 | 8,926,432 | 8 |
| DNS | 1120 × 840 × 280 | 71,411,456 | 1 |

**Table 1.** Resolution for various calculations.

| Model | Streamwise Reynolds stress | Cross-stream Reynolds stress | Spanwise Reynolds stress | Mass-fraction variance |
|---|---|---|---|---|
| Dynamic Smagorinsky (DSM) | -8% | 5% | 6% | -5.6% |
| Dynamic Gradient (DGM) | -11% | -2% | -4.3% | -7% |
| Dynamic mixed model (DMM) (Smagorinsky + Scale-similarity) | -15% | -2% | -4.3% | -10% |
| Dynamic Clark model (DCM) (Smagorinsky + Gradient) | 0% | 5% | 0.4% | -8% |

**Table 2.** Percentage error in peak prediction for the fine mesh LES.

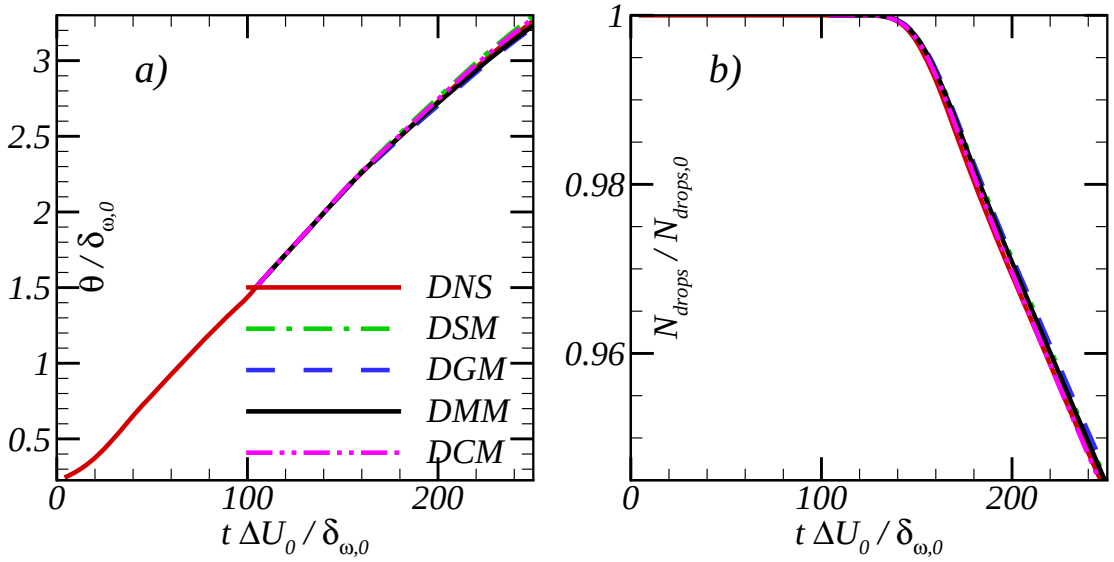


**Figure 1**. Temporal evolution of integral quantities: (a) Momentum thickness, (b) Number of drops. Fine grid.

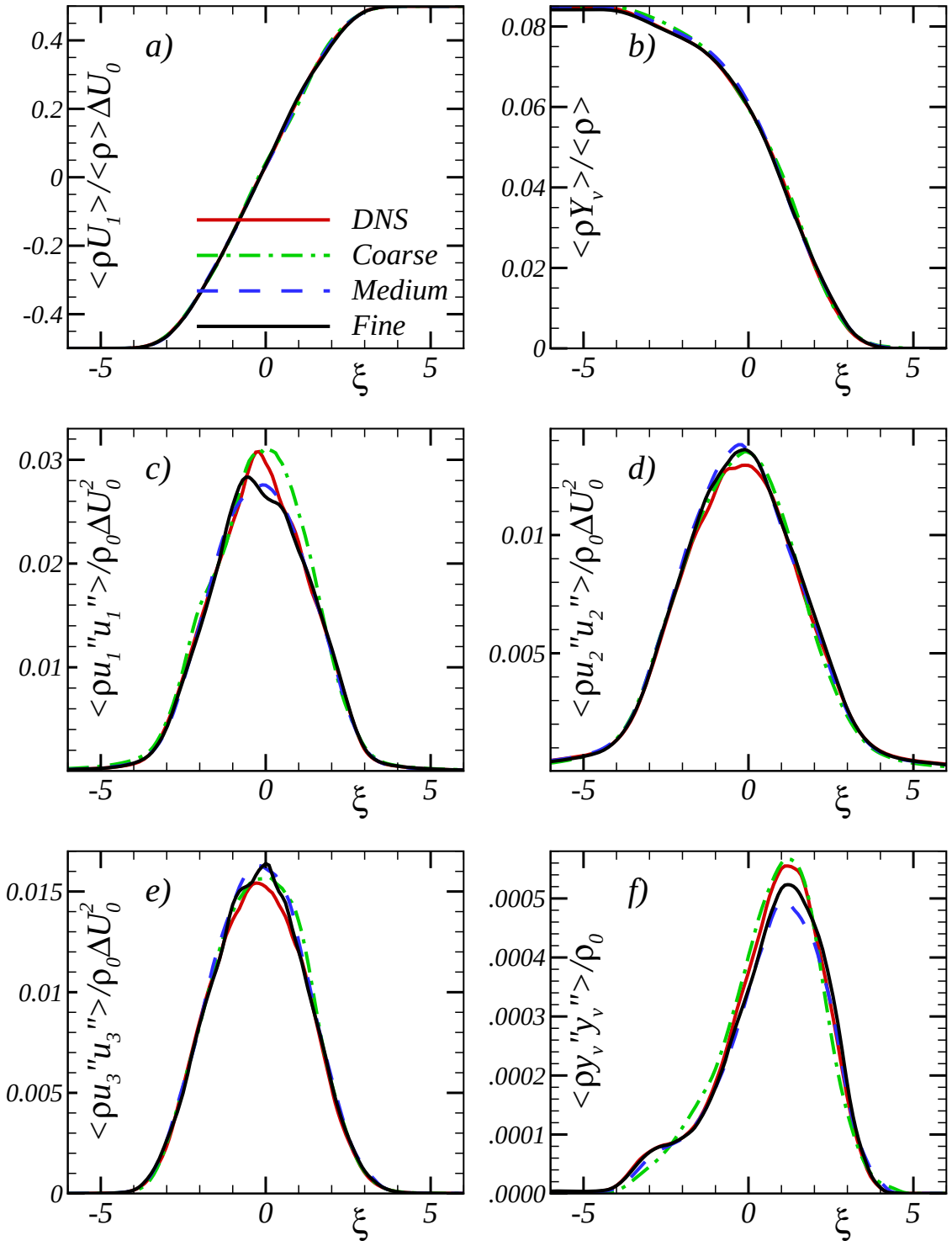


**Figure 2**. Cross-stream profiles for Dynamic Smagorinsky model: (a) Favre-averaged streamwise velocity, (b) Favre-averaged vapor mass fraction, (c) Streamwise Reynolds stress, (d) Cross-stream Reynolds stress, (e) Spanwise Reynolds stress, and (f) Variance of vapor mass fraction fluctuation.

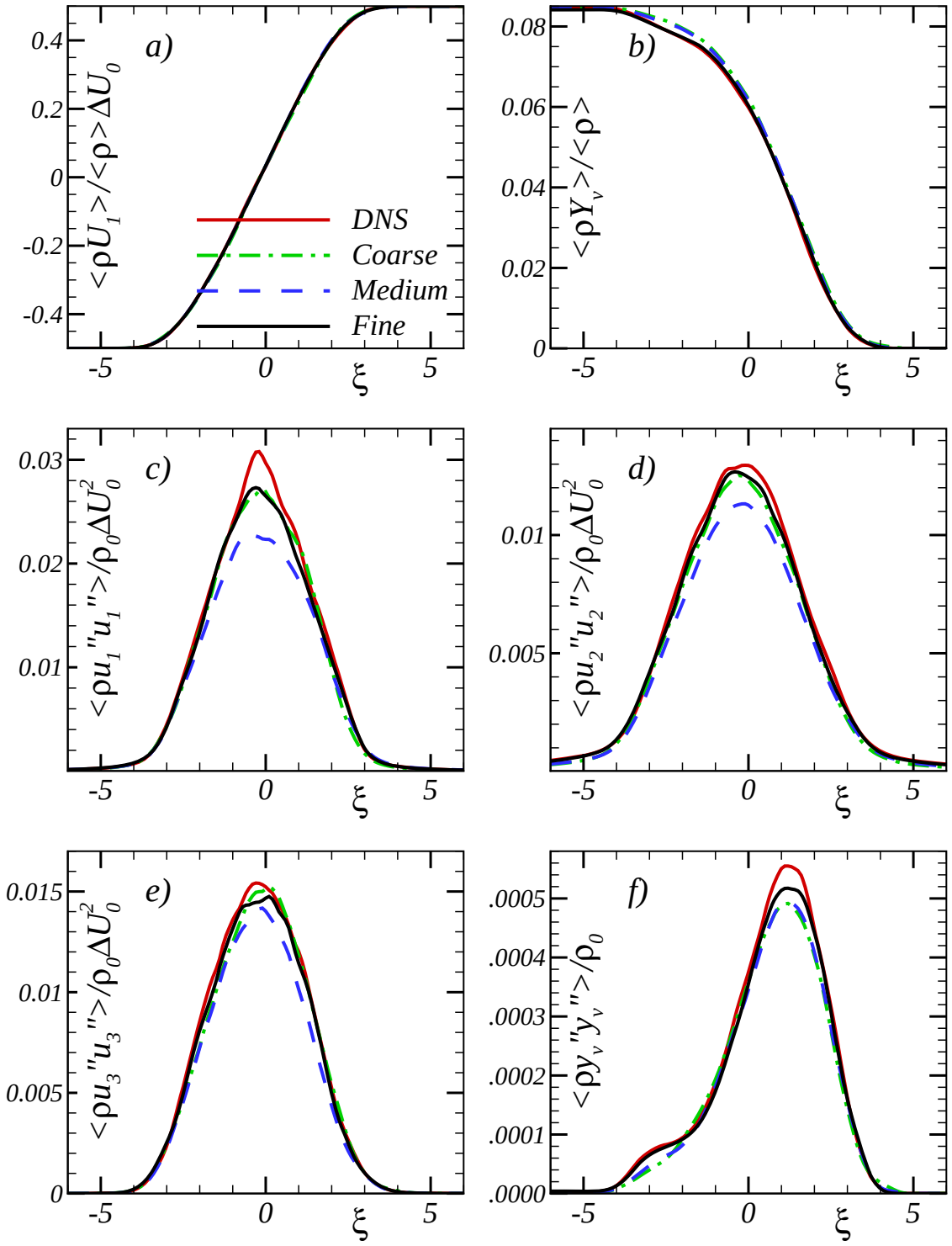


**Figure 3**. Cross-stream profiles for Dynamic Gradient model: (a) Favre-averaged streamwise velocity, (b) Favre-averaged vapor mass fraction, (c) Streamwise Reynolds stress, (d) Cross-stream Reynolds stress, (e) Spanwise Reynolds stress, and (f) Variance of vapor mass fraction fluctuation.

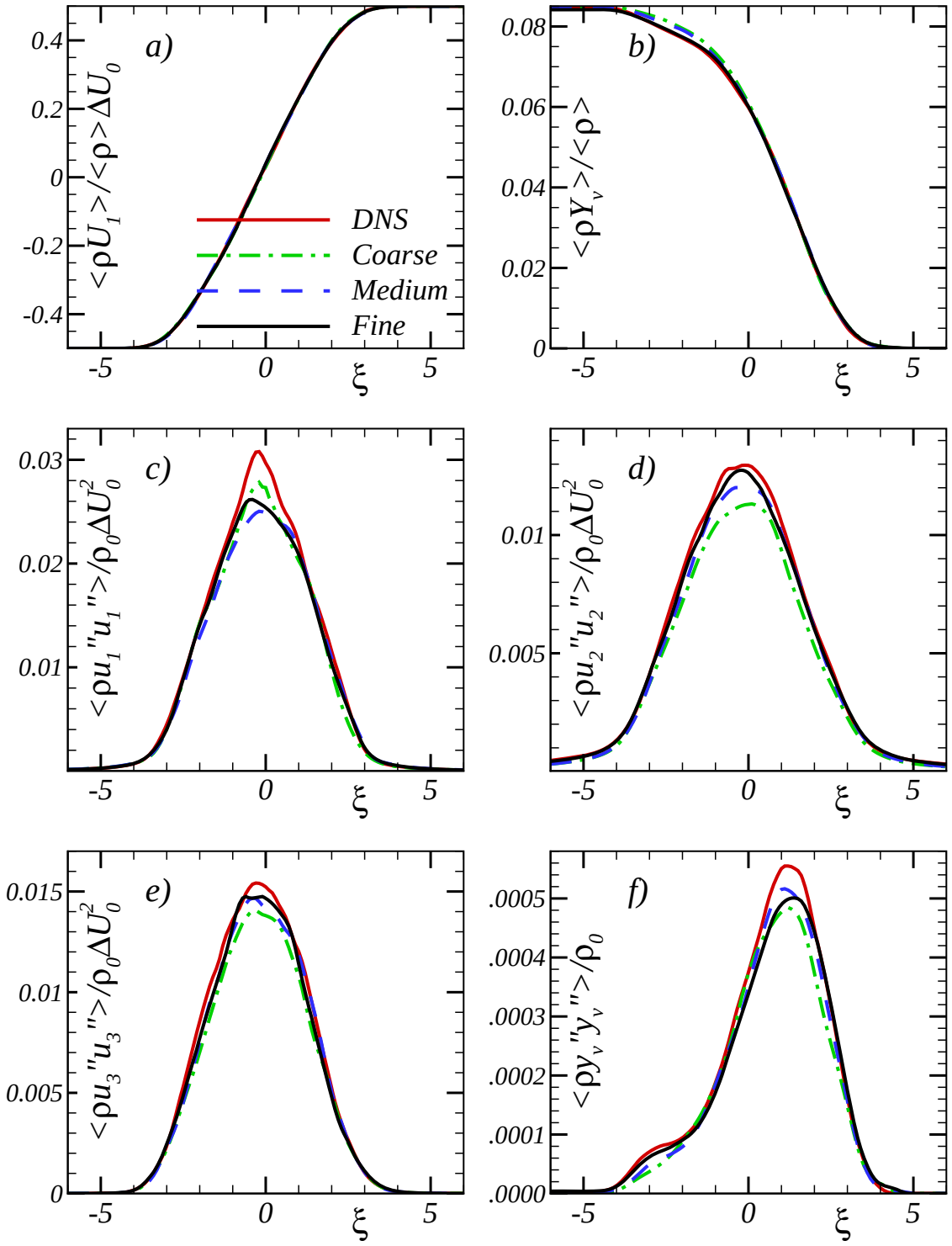


**Figure 4**. Cross-stream profiles for Dynamic Mixed model: (a) Favre-averaged streamwise velocity, (b) Favre-averaged vapor mass fraction, (c) Streamwise Reynolds stress, (d) Cross-stream Reynolds stress, (e) Spanwise Reynolds stress, and (f) Variance of vapor mass fraction fluctuation.

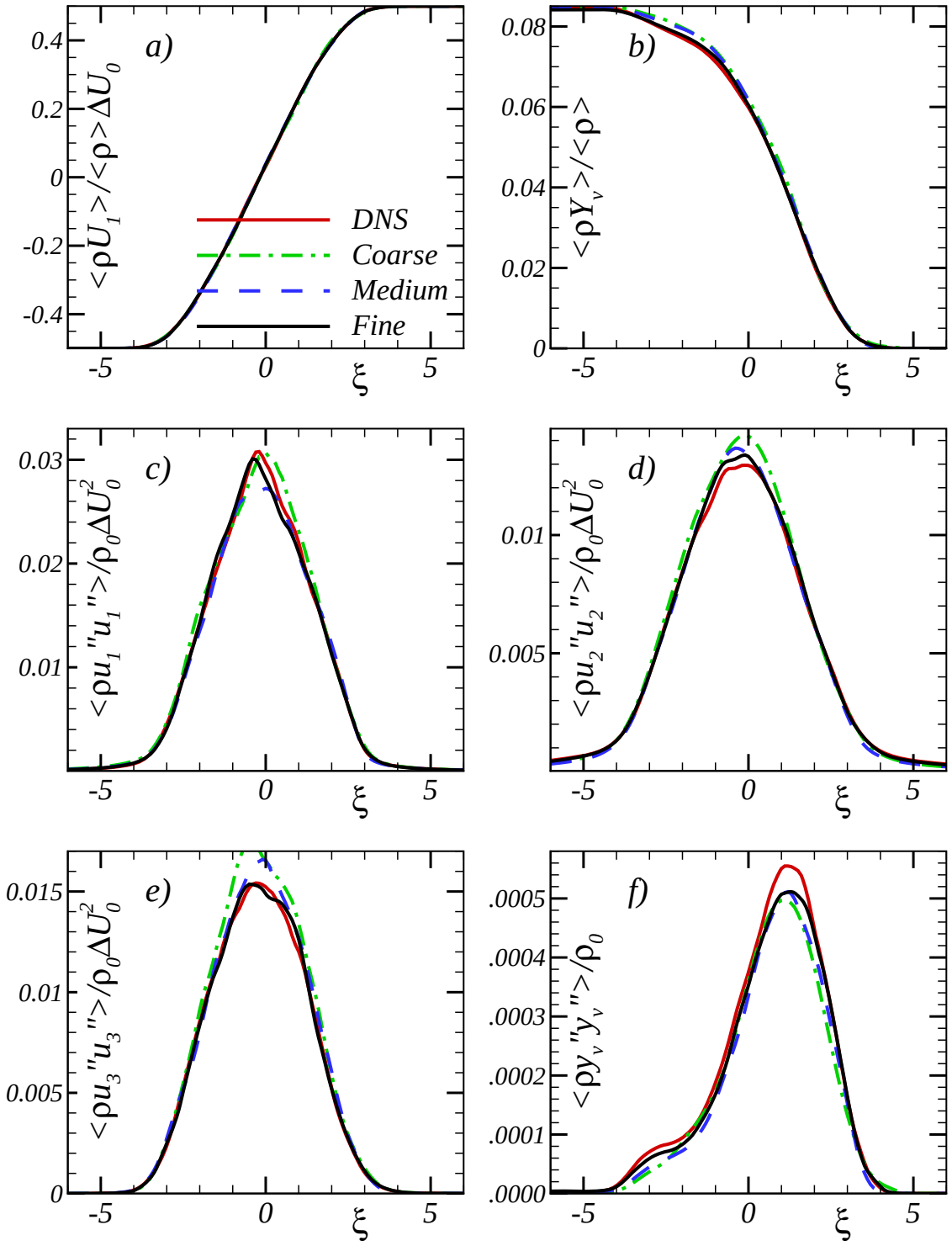


**Figure 5**. Cross-stream profiles for Dynamic Clark model: (a) Favre-averaged streamwise velocity, (b) Favre-averaged vapor mass fraction, (c) Streamwise Reynolds stress, (d) Cross-stream Reynolds stress, (e) Spanwise Reynolds stress, and (f) Variance of vapor mass fraction fluctuation.

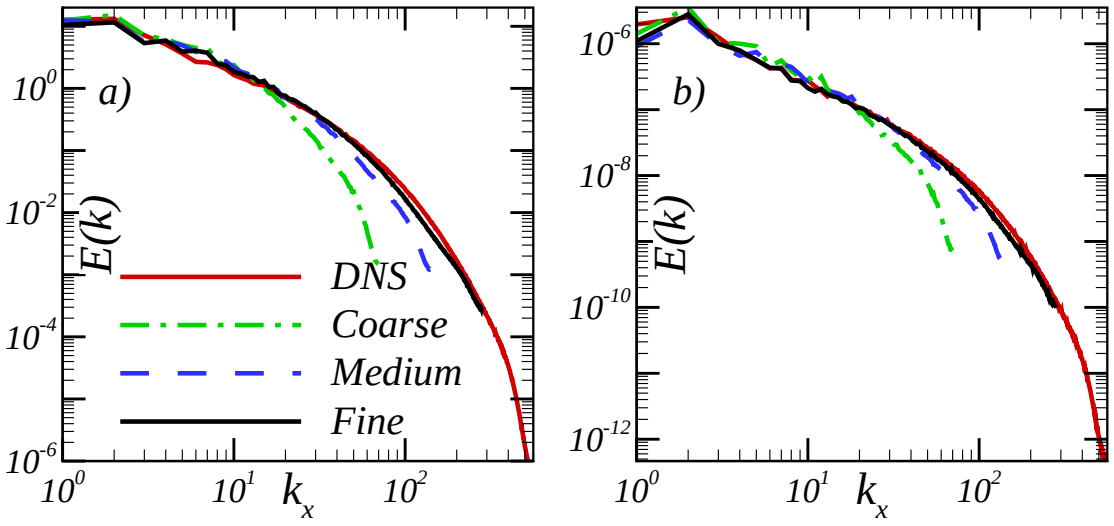


**Figure 6**. Streamwise spectra for Dynamic Smagorinsky model of: (a) Turbulent kinetic energy, (b) Vapor mass fraction fluctuation.

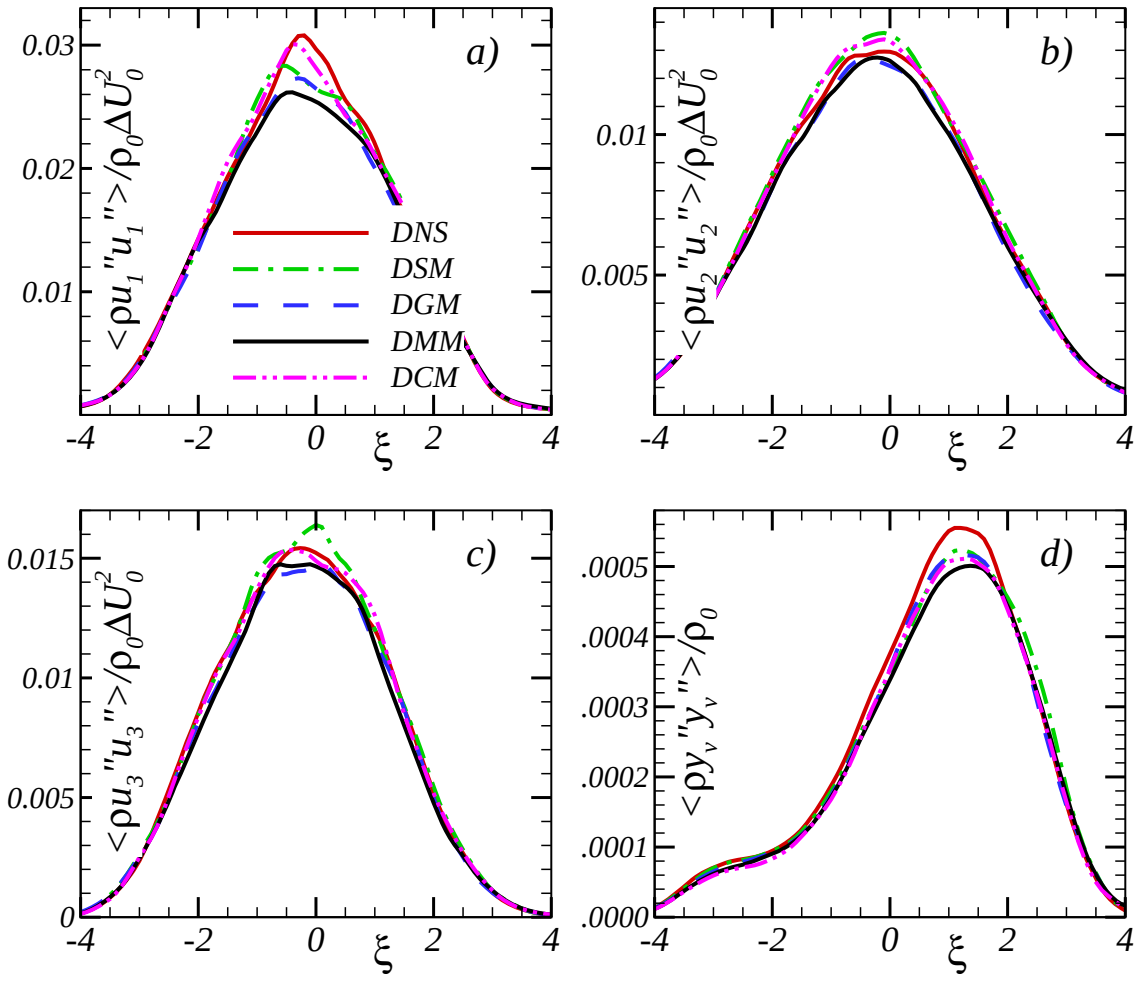


**Figure 7**. Cross-stream profiles for all the models: (a) Streamwise Reynolds stress, (b) Cross-stream Reynolds stress, (c) Spanwise Reynolds stress, and (d) Variance of vapor mass fraction fluctuations. Fine grid.

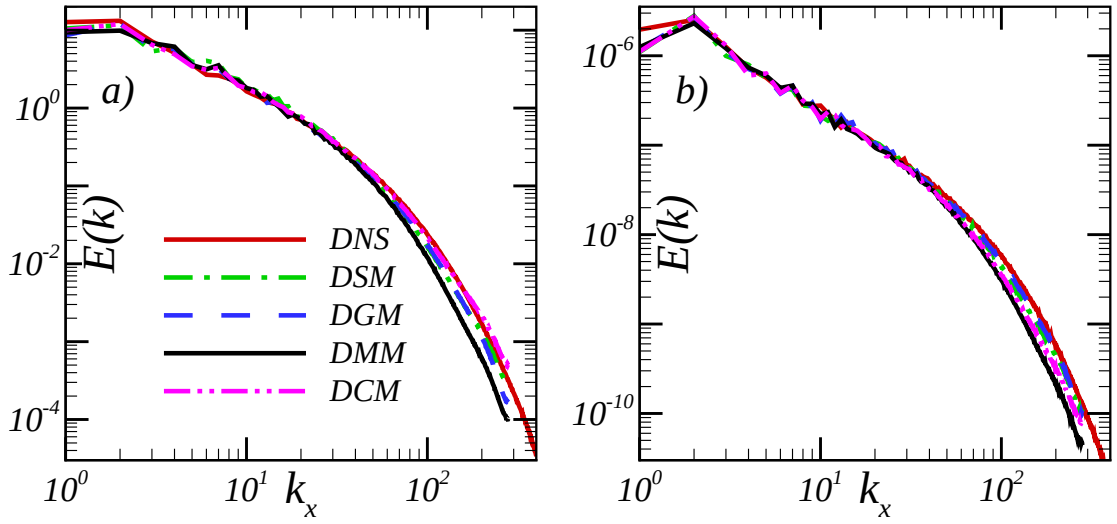


**Figure 8**. Streamwise spectra for all the models of: (a) Turbulent kinetic energy, (b) Vapor mass fraction fluctuation. Fine grid.

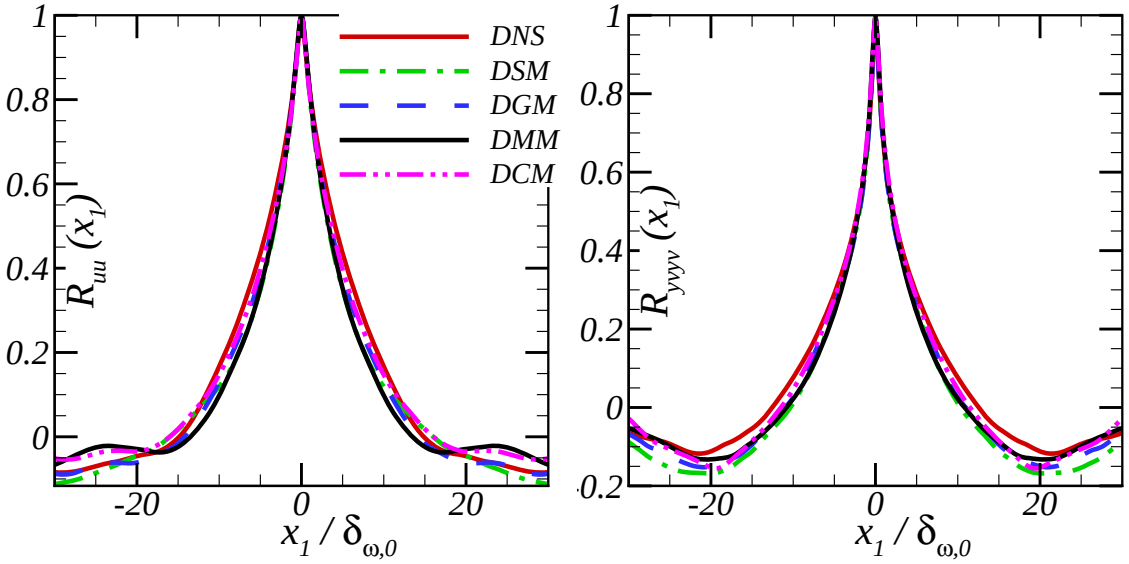


**Figure 9**. Two point streamwise correlations for all the models of: (a) Streamwise fluctuation, (b) Vapor mass fraction fluctuation. Fine grid.

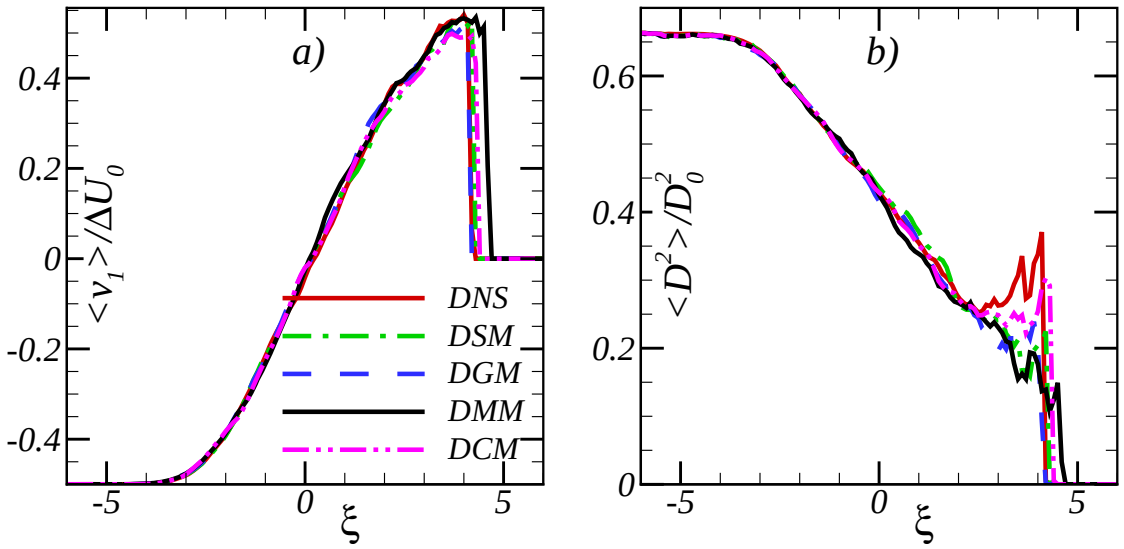


**Figure 10**. Cross-stream profiles for all the models: (a) Mean streamwise drop velocity, (b) Square of the average drop diameter. Fine grid.

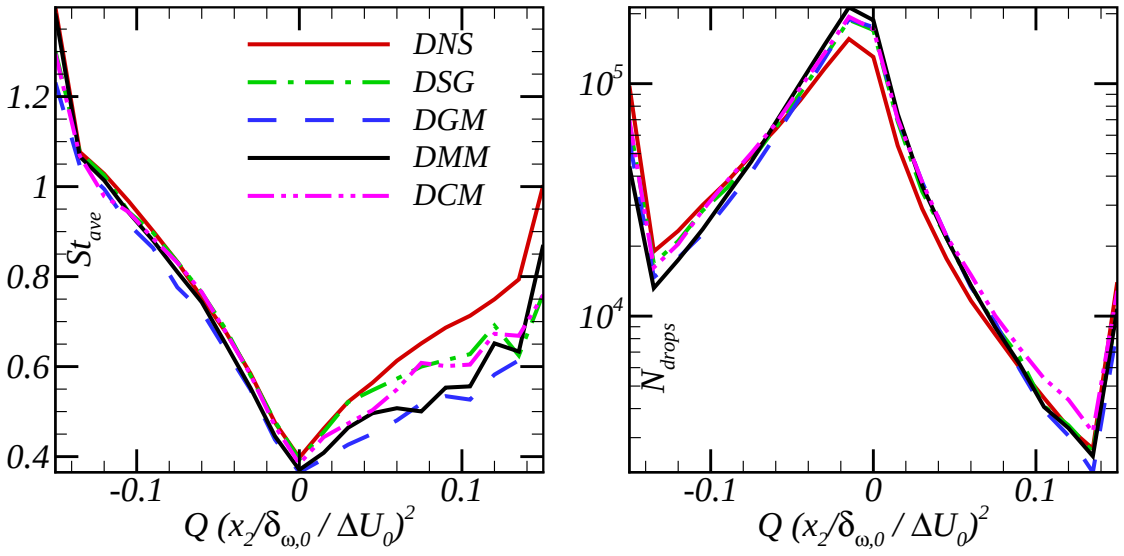


**Figure 11**. Profile of Stokes number conditioned with $Q$ and number of drops conditioned with $Q$ at $x_2/\delta_{\omega,0} = 0$. Fine grid.